

# Toward Predicting Performance of an Axial Flow Waterjet Including the Effects of Cavitation and Thrust Breakdown

Seth Schroeder<sup>1</sup>, Sung-Eun Kim<sup>1</sup>, Hrvoje Jasak<sup>2</sup>

<sup>1</sup>Naval Surface Warfare Center Carderock Division, West Bethesda, MD, US

<sup>2</sup>Wikki Ltd., London, UK

## ABSTRACT

Waterjet propulsion has gained increasing attention from the U.S. Navy in recent years. Waterjets enjoy several advantages over traditional screw propellers including shallow draft, increased maneuverability, and high-speed capability. Also in recent years, significant progress has been made in the prediction of waterjet performance with Reynold's Averaged Navier Stokes (RANS) based Computational Fluid Dynamics (CFD) tools. These predictions have included detailed analysis of torque and head rise values which are essential to the design and analysis of a waterjet system. The ultimate goal of the present work is to predict these values including the effects of cavitation and thrust breakdown using a Naval Surface Warfare Center Carderock Division (NSWCCD) internally developed version of a non-commercial RANS code. This paper outlines the preliminary progress that has been made towards this goal. The following sections outline the mesh generation and flow solver development, and give comparisons with the measured data at model scale. The waterjet of interest is the U.S. Navy Office of Naval Research's Axial-flow Waterjet One pump. The model scale test comparison calculations are made at several steady-state flow conditions for a rotor only case. The RANS solver developed in the study is based on the Open Field Operation and Manipulation (OpenFOAM) CFD library. The computational mesh was generated using the commercially available Ansys IcemCFD Hexa utility.

## Keywords

Waterjet, OpenFOAM, RANS, CFD, Cavitation

## 1 INTRODUCTION

Waterjet technology has become a popular choice for marine propulsion applications. The advantages of waterjets are numerous and include operability in shallow water, high-speed, and increased maneuverability. The shallow draft is a result of a completely internal flow pump whose inlet is flush with the hull of the ship. For example, in a very shallow draft configuration, it is only mandatory that the inlet be fully submerged. This allows waterjet craft to operate in water depth much less than their conventional screw

counterparts. Maneuverability is greatly increased by the thrust vectoring capability of waterjets. This vectoring is achieved by the use of steering buckets at the outlet of the waterjet.

Another advantage of waterjets over screw propellers is improved cavitation performance. With an internal flow system, the internal pressure throughout the system can be controlled with the shaping of the hub and casing. This control in pressure can delay cavitation inception. Cavitation inception brings the usual adverse side effects of noise, vibration, thrust breakdown, and ultimately damage due to erosion. Though waterjets have these advantages over traditional screw propellers, cavitation cannot be eliminated completely. Furthermore, any improvement in performance is the result of a well conducted design process, and makes the ability to predict cavitation during the design process of paramount importance to designers trying to maximize performance at a given power.

Significant progress has recently been made on predicting waterjet performance using Computational Fluid Dynamics (CFD). Accurate performance predictions have been shown by Brewton et al. (2006). This past study used an unstructured meshing scheme to model the Center for the Commercial Development of Transportation Technologies (CCDoTT) waterjet using Fluent. The authors of this past work concluded that Reynolds Averaged Navier Stokes (RANS) solvers have a place in the design process of waterjets. It was also concluded that future steps of RANS waterjet analysis should utilize a cavitation model.

The ultimate goal of the present study is to predict waterjet performance affected by cavitation. The following approach differs from the previous study in two main ways. First, a structured hexahedral approach is taken for mesh generation. Second, in lieu of commercial CFD codes, CFD codes developed in-house using an open-source CFD tool-kit are used for the analysis to gain the advantage of code development and manipulation.

The first obstacle for cavitation prediction using CFD is mesh generation. While an unstructured tetrahedral mesh offers ease of generation, especially for

the complex geometry involved, they are prone to excessive numerical dissipation. A structured mesh offers advantages in that respect. However, the complex geometry of the hub, duct, and blade sections are difficult to model with a structured hexahedral mesh approach. Because of the high pitch angles of the blade sections, a hexahedral mesh can have highly skewed elements close to the surface. Highly skewed elements should be avoided as much as possible, since they lead to poor solution convergence or outright divergence.

The use of an open-source RANS code is beneficial in that the code can be modified and developed to meet the desired application needs. For this study, the authors made use of the Open Field Operation and Manipulation (OpenFOAM) CFD toolbox. OpenFOAM is an open source library of C++ modules and solvers that can be modified and assembled to create desired solvers.

The main objective of this work is to evaluate the ability of a RANS code to predict thrust and torque on the Office of Naval Research's Axial-flow WaterJet One (ONR AxWJ-1) pump (Michael *et al.*, 2008). The following sections detail the methods used for grid generation, solver development, and solution strategies. Results also follow for code validation, and comparison with steady state test results as well as potential flow simulation results (Sun, 2008).

## 2 ANALYSIS

The waterjet of interest is the ONR AxWJ-1. This is a pump designed by the Naval Surface Warfare Center Carderock Division for test and evaluation purposes. The pump geometry consists of seven right-handed rotor blades and eleven stator blades. The upstream shaft has a diameter of 0.0508 meters (2 inches). The hub, which begins as its diameter increases from the shaft, has an axial length of 0.3048 meters (12 inches). The diameter of the casing is also 0.3048 meters (12 inches). Currently this design is undergoing testing at Johns Hopkins University (JHU) through support of the Office of Naval Research (Wu *et al.*, 2008). The ONR AxWJ-1 is shown below in Figure 1.

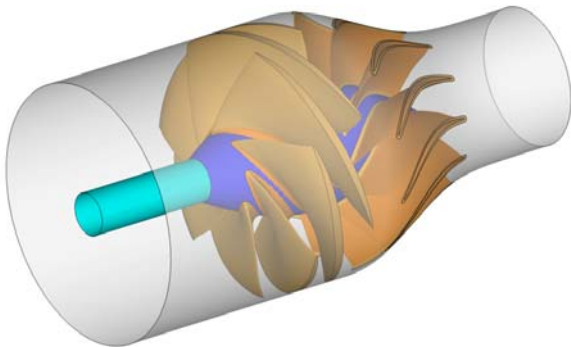


**Figure 1 – Image of ONR AxWJ-1**

For the early development of this cavitating RANS capability, a rotor only domain is used. The

design condition is a flow coefficient ( $Q^*$ ) value of 0.38 at 900 RPM, where  $Q^*$  is defined as:

$$Q^* = \frac{Q}{nD^3} \quad (1)$$

Where  $Q$  = volumetric flow rate [ $m^3/s$ ];  $n$  = rotations per second [ $1/s$ ]; and  $D$  = rotor diameter [ $m$ ].

This design point corresponds to a dimensional inlet velocity of 2.22 m/s. The working fluid is fresh water with a density of 998.2  $kg/m^3$ , and a kinematic viscosity of 1.00481E-06  $m^2/s$ . This design point corresponds to a Reynold's number of approximately 6.5e5 at a span of 0.9R, where R is the rotor radius.

### 2.1 Grid Generation

The grid generation package of choice for this study is Ansys' IcemCFD Hexa. To compliment the cavitation model as much as possible, a structured hexahedral meshing scheme is used. ICEM allows for structured mesh generation through a top-down blocking approach. This strategy also reduces the number of cells in the domain relative to a comparable unstructured tetrahedral mesh. To further reduce the mesh size and computational time, only a single blade passage is modeled with periodic boundary conditions employed.

The main challenge when considering a structured mesh of a rotor blade is in the extreme pitch angle of the blade. This geometry leads to poor quality, highly skewed cells along the blade. These cells cause numerical instabilities in regions critical to the solution of the domain. To reduce the skewness of the cells near the blade, thus increasing quality, a cyclic general grid interface (GGI) algorithm based on interpolation is used at the periodic boundaries. This interpolation allows the periodic boundaries to be non-conformal and provides much flexibility in generating the structured mesh. The difference between these two approaches to periodic boundaries is illustrated below in Figure 2 and Figure 3. In these figures, a two-dimensional blade cross section is shown with periodic boundaries running parallel to the chord of the section. Two notional grid lines are shown in each figure. In the conformal periodic case, each gridline must map to the same axial-coordinate on the periodic boundaries. This leads to the highly skewed elements near the blade surface. In the non-conformal figure, it is seen that flexibility on the periodic boundary allows for gridlines orthogonal to the blade surface.

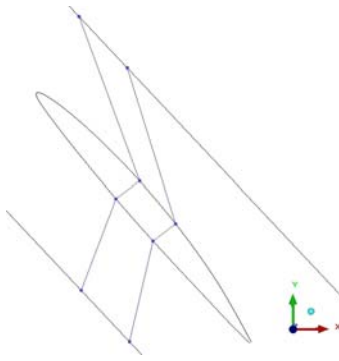


**Figure 2 – Illustration of the Conformal Periodic Boundaries**

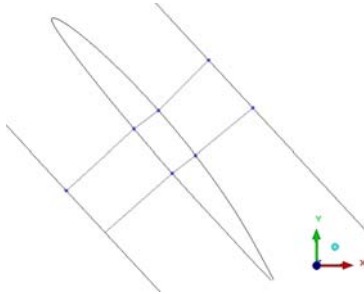


**Figure 3 – Illustration of the Non-conformal Periodic Boundaries**

The authors plan to carry out a mesh dependency study as part of this ongoing work. One of the computational meshes, whose results will be presented in this paper, consists of a domain that spanned the length of the hub. This grid has an inlet plane at approximately 1 radius in front of the leading edge of the rotor blade and an outlet plane approximately 1 diameter behind the trailing edge of the rotor blade. The cell count for this smaller domain is approximately 1 million cells. An illustration of the surface mesh on the blade and hub, copied rotationally for visualization, is shown below in Figure 4.

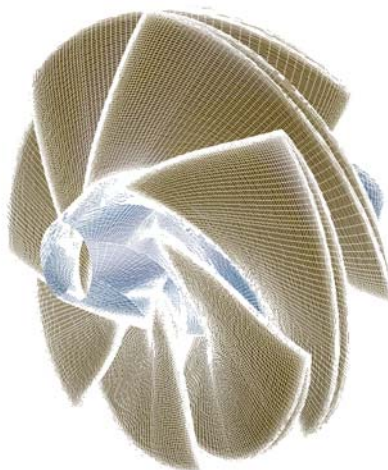


**Figure 4 – Illustration of the Hub and Rotor Surface Mesh**

The  $y^+$  values on the blade surface at the design condition range from less than 1 to a maximum value of approximately 50, and averaged approximately 10. A histogram of the wall  $y^+$  values on the blade surface at

the design condition is shown in Figure 5. Wall  $y^+$  is defined as:

$$y^+ = \frac{\rho u_\tau y}{\mu} \quad (2)$$

where  $u_\tau$  = friction velocity, and  $y$  = distance to the wall.

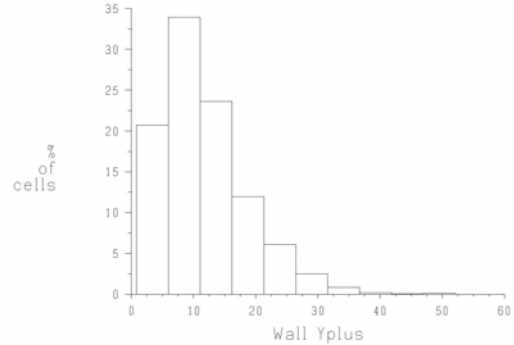


**Figure 5 - Histogram of wall  $y^+$  values on the blade surface**

## 2.2 The Flow Solver

The use of OpenFOAM facilitates rapid development of flow solvers tailored to propulsor applications. The solver used here belongs to the Multiphase Computational Fluid Dynamics (MCFD) solver suite (Kim, 2008) which has been developed at Carderock over the years using the OpenFOAM tool-kit. The CFD solvers in OpenFOAM employ a cell-centered finite-volume method based on a multi-dimensional linear reconstruction scheme that permits use of computational elements (cells) with arbitrary polyhedral cell topology including quadrilateral, hexahedral, triangular, tetrahedral, pyramidal, prismatic, and hybrid meshes. The solution gradients at cell centers can be evaluated by applying Green-Gauss theorem or by least-square method. For discretization of convection terms in the momentum and turbulence equations, a second-order-accurate upwind scheme was used. The SIMPLE algorithm is used for velocity-pressure coupling for all the steady, single-phase flow computations discussed in this paper. The discretized governing equations are solved using point-implicit Gauss-Seidel relaxation along with an algebraic multi-grid (AMG) method to accelerate solution convergence.

The solver permits use of Single Rotating Frame of reference (SRF) by which the effects of the system rotation are accounted for by the body forces in the momentum equations due to centrifugal and Coriolis forces. The flow is assumed rotationally cyclic, which allows one to model a single blade passage only. The General Grid Interface (GGI) capability available in the extended version of OpenFOAM V1.5 permits use of non-matching periodic boundaries, which leads to higher quality cells.

A number of RANS turbulence models including  $k-\epsilon$  and  $k-\omega$  families are available for use with the solvers. Some of the RANS model implementations in the original library have been modified so that they are numerically

more robust. In addition, a new version of  $k-\omega$  model, namely, Wilcox' 1998  $k-\omega$  model, has been added to the existing RANS model library. Both realizable  $k-\varepsilon$  and  $k-\omega$  are used to make a comparison to each other and to the test data.

### 2.3 Solution Strategies

The boundary conditions included an upstream set velocity inlet which was non-uniform to account for the addition of a turbulent boundary layer. This boundary condition allowed for a study with the upstream conditions impacting the rotor only solution. The downstream outlet was set to have a fixed pressure gradient. The periodic boundaries of the single blade passage were interpolated using the previously mentioned General Grid Interface (GGI).

To improve the convergence, the solution is started using a first-order upwind scheme and a relatively heavy under-relaxation factor. The initial guess of the velocity field was found to significantly affect the solution convergence. Given the initial guess for the velocity field in the absolute frame of reference, the relative velocity field was obtained by a transformation accounting for the system rotation. Typically, the switch back to the high-order discretization schemes and the high under-relaxation factors was made after approximately one hundred iterations. The computational runs were made for a range of flow rates. These conditions correspond to the steady state conditions that were measured at the JHU water tunnel (Wu *et al.*, 2008).

## 3 RESULTS AND DISCUSSION

The computational results can be compared to the measured data through global parameters such as torque and head rise. The differing turbulence models are compared to one another through detailed flow features such as pressure distributions and contours.

### 3.1 General Comparison to Test Data

Torque data is compared between the calculations and the experimental data non-dimensionally by use of a torque coefficient,  $K_Q$ , which is defined as:

$$K_Q = \frac{\text{torque}}{\rho n^2 D^5} \quad (3)$$

Where  $n$  = rotations per second [1/s]; and  $D$  = rotor diameter [m].

The comparison of torque data is shown in Figure 6.

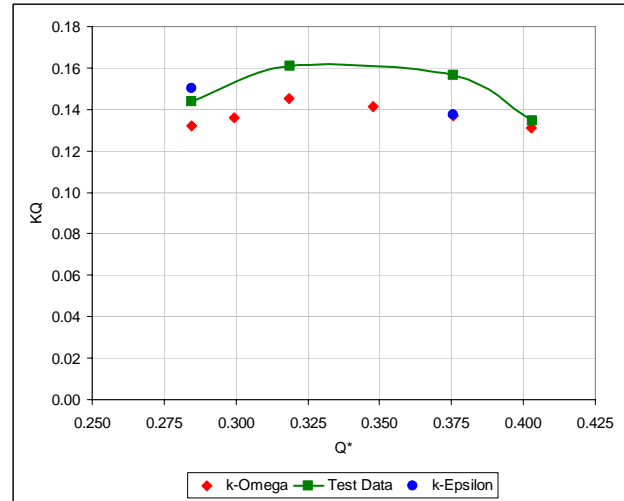


**Figure 6 – A Comparison of Experimental and Computational Torque Results for  $k-\omega$  and  $k-\varepsilon$  Turbulence models**

In Figure 6, a comparison is made between the test data and the two different turbulence models used in the calculations. The two turbulence models used are the realizable  $k-\varepsilon$  model (Shih *et al.*, 1995) and Wilcox  $k-\omega$  model (Wilcox, 1998). Both turbulence model results are shown at the design point of  $Q^* = 0.38$ , as well as at one off design condition of  $Q^* = 0.28$ . At the design condition,  $K_Q$  is predicted approximately 10% low by both turbulence models. However, at the lower flow rate off design condition, the Realizable  $k-\varepsilon$  model predicted slightly higher than the test data while the Wilcox'  $k-\omega$  model predicted slightly lower. Despite the discrepancy, Wilcox'  $k-\omega$  model reproduces the trend – the drop of  $K_Q$  at the lower flow-rate.

The laboratory test setup has a sudden expansion in the discharge chamber which is located downstream of the nozzle section. This sudden expansion is not included in the computational model used in our preliminary calculations. This prevents a direct comparison of head rise as the experimental results measure downstream pressure at this location. The experimental test setup as given by Wu *et al.* is shown in Figure 7.

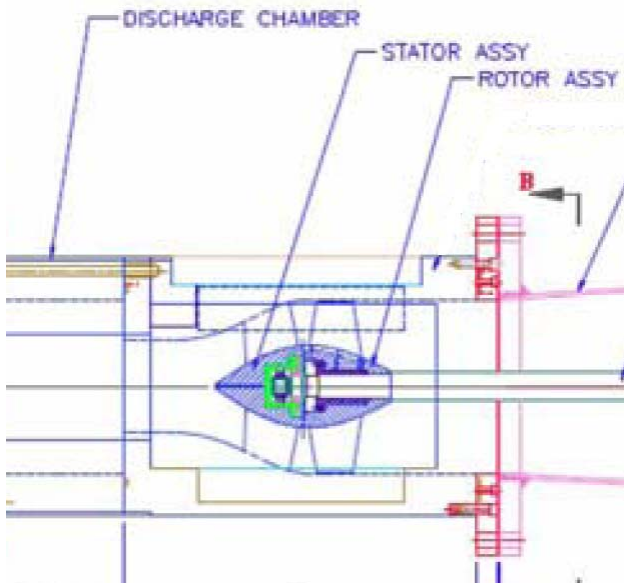


Figure 7 – Sketch of the JHU Experimental Test Setup (Wu *et al.*, 2008)

It is believed the differences in torque between the measurements and the predictions are attributable to the differences in handling the near-wall mesh solution. The realizable  $k-\epsilon$  model in the OpenFOAM library is strictly a high Reynolds number model that cannot account for viscous effects in the laminar sublayer when used with a fine near-wall mesh. In contrast, the  $k-\omega$  turbulence model is nominally a legitimate low-Re models which can be used to integrate all the way to the wall. As previously shown in Figure 5, the preliminary mesh split the difference between the two turbulence models with a  $y^+$  mainly in the buffer region of 5-30.

### 3.2 General Comparison to Potential Flow results

Potential flow results were obtained from Professor Spyros Kinnas' Ocean Engineering Group at the University of Texas (Sun *et al.* 2008). These results are shown in Figure 8.

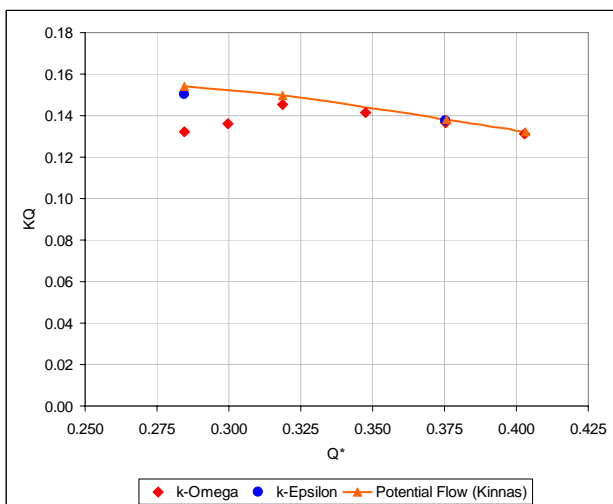


Figure 8 - A Comparison of Potential Flow and RANS Computational Torque Results for  $k-\omega$  and  $k-\epsilon$  Turbulence models

It is seen in Figure 8 that the two sets of computational results match fairly well. The main discrepancy occurs with the Wilcox  $k-\omega$  model at the lower off-design flow rates.

### 3.3 Detailed Turbulence Model Comparison

The main difference in torque measurements between the two turbulence models is seen in the handling of pressure vs. viscous forces, and can be seen by comparing the percentage of total torque that each force constitutes. At the design condition, the Wilcox  $k-\omega$  model predicts more than twice the viscous force as percentage of total torque when compared to the Realizable  $k-\epsilon$  model. This can be seen below in Figure 9. Based on previous waterjet publications, the Wilcox  $k-\omega$  model seems to have too high a percentage of viscous torque for this application.

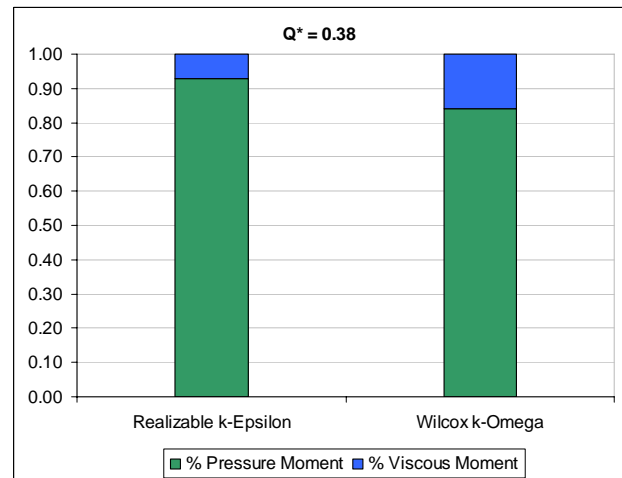


Figure 9 – A Comparison of the Pressure and Viscous Moment as a Percentage of Total Torque Predictions of the  $k-\omega$  and  $k-\epsilon$  Turbulence models

To study the differences seen at the off-design condition of  $Q^* = 0.28$ , the authors found it useful to study the pressure coefficients on the blade surfaces. The results of pressure coefficient contours on the pressure side of the rotor blade can be seen in Figure 10 and Figure 11 for the Wilcox  $k-\omega$  turbulence model and the realizable  $k-\epsilon$  turbulence model, respectively. Pressure coefficient,  $C_p$ , is defined as:

$$C_p = \frac{p - p_\infty}{\frac{1}{2} \rho n^2 D^2} \quad (4)$$

where  $p$  = pressure,  $n$  = rotations per second [1/s]; and  $D$  = rotor diameter [m].

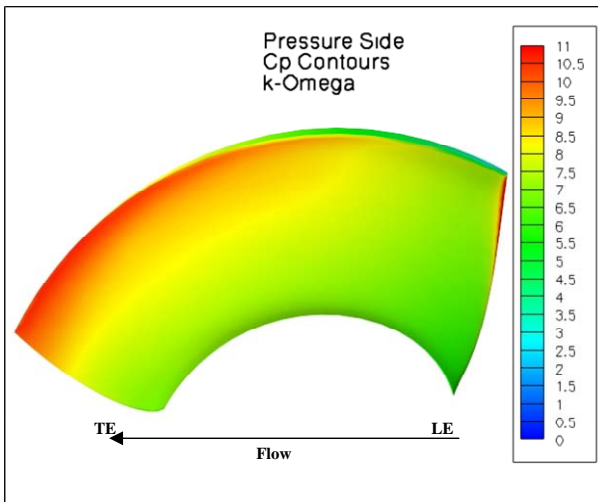


Figure 10 - Pressure Side Cp Contours, Wilcox  $k-\omega$  Turbulence Model,  $Q^*=0.28$

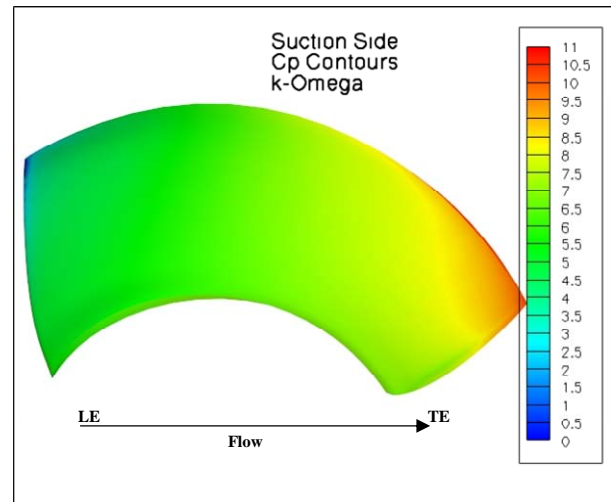


Figure 12 - Suction Side Cp Contours, Wilcox  $k-\omega$  Turbulence Model,  $Q^*=0.28$

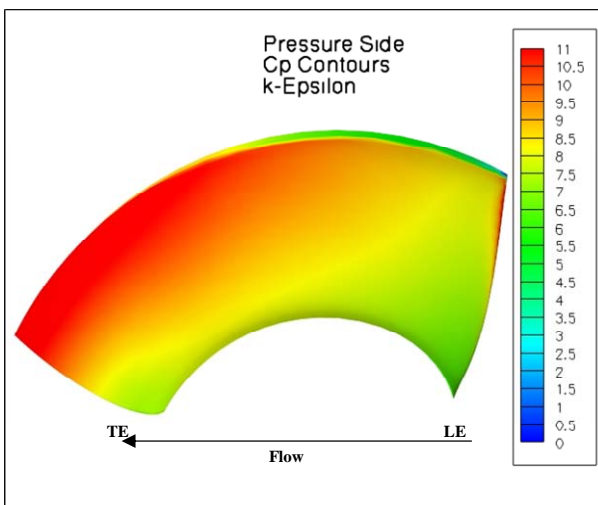


Figure 11 - Pressure Side Cp Contours, Realizable  $k-\epsilon$  Turbulence Model,  $Q^*=0.28$

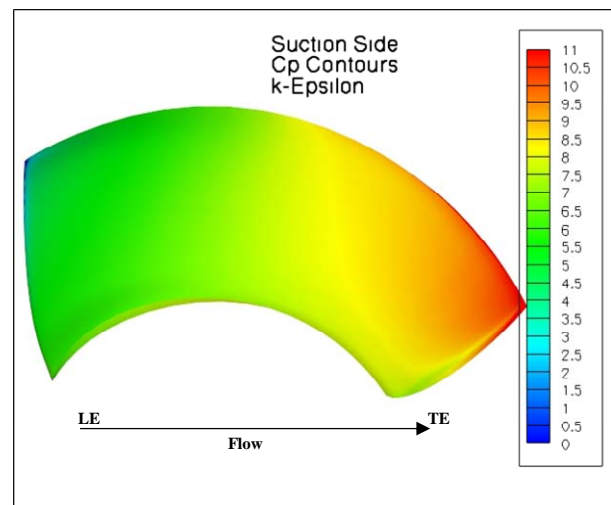


Figure 13 - Suction Side Cp Contours, Realizable  $k-\epsilon$  Turbulence Model,  $Q^*=0.28$

It is seen in the pressure side pressure coefficient contours that pressure remains significantly higher throughout the blade surface when the Realizable  $k-\epsilon$  turbulence model is employed. This suggests that the two turbulence models do not handle the off-design angle of attack similarly.

The suction side pressure coefficient contours are shown in Figure 12 and Figure 13 for the Wilcox  $k-\omega$  and Realizable  $k-\epsilon$ , respectively.

While the  $k-\epsilon$  model also shows generally higher pressure on the suction side of the blade, it appears that the relative difference is not as large as the pressure side. This result suggests that more lift is being predicted which explains the higher torque value reported by the  $k-\epsilon$  turbulence model. This finding is demonstrated in an even more quantitative manner in Figure 14 through Figure 16 where the chordwise pressure distributions are shown.

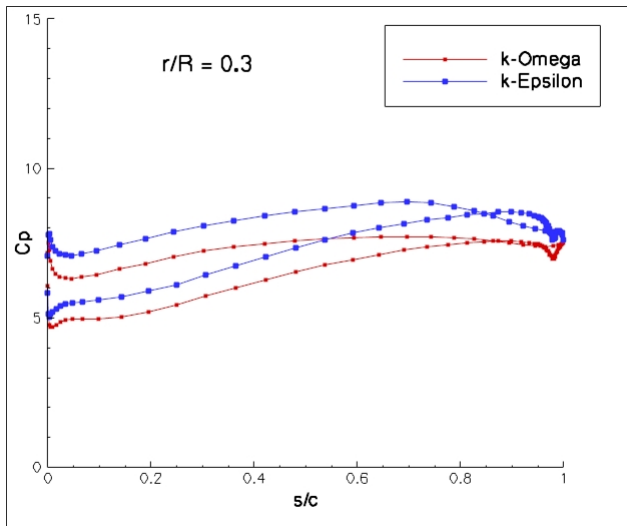


Figure 14 – Plot of Cp Distributions at  $r/R = 0.3$ ,  $Q^*=0.28$  for the  $k-\omega$  and  $k-\epsilon$  Turbulence models

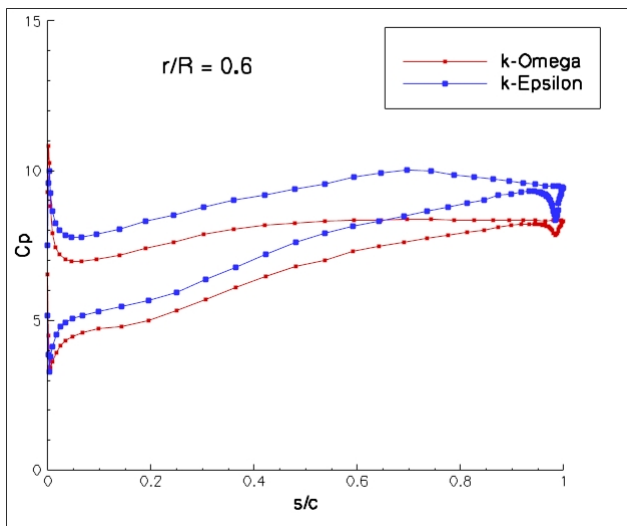


Figure 15 – Plot of Cp Distributions at  $r/R = 0.6$ ,  $Q^*=0.28$  for the  $k-\omega$  and  $k-\epsilon$  Turbulence models

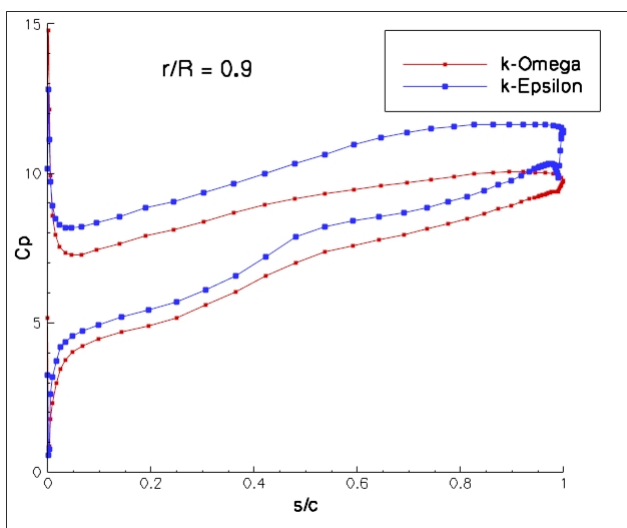


Figure 16 – Plot of Cp Distributions at  $r/R = 0.9$ ,  $Q^*=0.28$  for the  $k-\omega$  and  $k-\epsilon$  Turbulence models

#### 4 CONCLUSIONS

The preliminary solutions at off-design conditions are highly dependent on the turbulence model employed by the solver. It is also believed that the turbulence models fidelity will be highly dependent on mesh resolution, particularly in the near wall region.

It is seen from Figure 5 that the vast majority of  $y^+$  values on the blade surface fall in the buffer region ( $y^+ = 5 - 30$ ). The mesh used for our preliminary study thus is not ideal for the  $k-\epsilon$  model or  $k-\omega$  model employed in this study. It is surmised that the cells on the rotor blade could have led to numerical errors in the calculation. As stated previously, the Wilcox  $k-\omega$  model can be used to integrate to the wall. The above  $y^+$  values are too high for the Wilcox  $k-\omega$  model. In contrast, for the Realizable  $k-\epsilon$  model, used for high Reynold's number modeling, the above  $y^+$  values are too low for a proper solution.

Another possible source of error lies at the inlet of the rotor domain. It can be seen in Figure 7 that the experimental test section has an inlet that is still contracting as close as one radius from the rotor blade. The computational domain extended approximately one radius upstream and had a zero pressure gradient boundary condition. This boundary condition and domain may not correctly represent the experimental setup.

#### 5 FUTURE WORK

The next step for this study is to adapt the mesh to better accommodate each of the turbulence models by adjusting cell spacing for  $y^+$  values that were mentioned. Further steps will include steady-state calculations including a stator which will lead to cavitation calculations in which thrust breakdown is predicted.

#### 6 ACKNOWLEDGEMENTS

The authors would like to thank Dr. Ki-Han Kim for his continuous support and encouragement of this work through the Office of Naval Research.

The measured data used for comparison and validation was collected by Professor Joe Katz of John Hopkins University.

#### REFERENCES

- Brewton, S., Gowing, S., & Gorski, J. (2006). 'Performance Predictions of a Waterjet Rotor and Rotor/Stator Combination Using RANS Calculations'. Proceedings of the 26<sup>th</sup> Symposium on Naval Hydrodynamics, Rome, Italy.
- Kim, S.E. and Brewton, S. (2008). 'A Multiphase Approach to Turbulent Cavitating Flows,' Proceedings of the 27<sup>th</sup> Symposium on Naval Hydrodynamics, Seoul, Korea.

- Shih, T.-H., Liou, W.W., Shabbir, A., and Zhu, J. (1995). 'A New k- $\epsilon$  Eddy-Viscosity Model for High Reynolds Number Turbulent Flows - Model Development and Validation,' *Computers & Fluids*, Vol. 24, No. 3, pp. 227-238.
- Wilcox, D.C. (1988). *Turbulence Modeling for CFD*, 2<sup>nd</sup> Edition, DCW Industries, Inc.
- Wu, H., Soranna, F., Michael, T., Katz, J., Jessup, S. (2008) 'Cavitation Visualizes the Flow Structure in the Tip Region of a Waterjet Pump Rotor Blade', Proceedings of the 27<sup>th</sup> Symposium on Naval Hydrodynamics, Seoul, Korea.
- Sun, H., Kinnas, S. (2008) 'Performance Prediction of Cavitating Water-Jet Propulsors Using a Viscous/Inviscid Interactive Method', Transactions of the 2008 Annual Meeting of the Society of Naval Architects and Marine Engineers, Houston, Texas.
- Michael, T., Schroeder, S., Becnel, A. (2008). 'Design of the ONR AxWJ-2 Axial Flow Water Jet Pump', NSWCCD Department Report.